

COVER PAGE

Document downloaded by @DAEL

Sun Nov 29 21:41:50 2026
For personal use

When automatic English translation is provided, only the original document is authentic.
The EAA cannot be held responsible of any translation error

Bibliographical reference

A Meshfree Radial Point Interpolation Coupled with Infinite Acoustic Wave Envelope Element Method for Computing Acoustic Fields, Shaowei Wu, Yang Xiang and Jiachi Yao, Acta Acustica **vol. 104** (Number 1), 2018, pp. 64-78

DOI
https://doi.org/10.3813/AAA.919146

ACTA ACUSTICA UNITED WITH ACUSTICA
Vol. 104 (2018) 64 – 78
DOI 10.3813/AAA.919146

A Meshfree Radial Point Interpolation Coupled with Infinite Acoustic Wave Envelope Element Method for Computing Acoustic Fields

Shaowei Wu[1,2], Yang Xiang[1,2], Jiachi Yao[1,2]
[1)] Key Laboratory of High Performance Ship Technology (Wuhan University of Technology), Ministry of Education. yxiang@whut.edu.cn
[2)] School of Energy and Power Engineering, Wuhan University of Technology, Wuhan 430063, China.

Summary
To take advantage of the meshfree method in computational accuracy, the meshfree radial point interpolation method (RPIM) is introduced to compute acoustic fields in infinite domain. A hybrid meshfree-infinite acoustic wave envelope element method is proposed for acoustic radiation prediction. To improve the accuracy, soften the system stiffness compared to the "overly-stiff" finite element method, and properly model the amplitude decay of the outgoing travelling wave, the RPIM in near field is combined with a variable-order infinite acoustic wave envelope element (WEE) in far field to establish the discretized system equations. The coupling of the PRIM and WEE is achieved by interface elements to maintain the continuity and compatibility on the interface between the two domains, where the RPIM and WEE methods are applied. The suitable shape parameters of radial basis functions and the size of the influence domain, which influence the performance of this method, are determined by numerical experiments. From the numerical results, the method not only can provide data with high accuracy but also has a faster convergence speed than the conventional method of the finite element method (FEM) combined with WEE. The method can take full advantage of both the RPIM and WEE methods. The experimental results show that the method is very flexible for acoustic radiation prediction in the infinite domain.

PACS no. 43.20.Rz, 43.40.At, 43.40.Rj

1. Introduction

Boundary element method (BEM) is established as a well-known numerical tool for predicting the sound pressure in an infinite domain. In the BEM, boundary surface discretization is only required, and the Sommerfeld radiation condition at infinity is naturally satisfied. Thus, a relatively small systems of equations is formed, with the advantage of obtaining solutions over a (d-1)-dimensional domain that is of one dimension lower than the original d-dimensional one [1, 2, 3]. However, the system matrices of BEM are usually non-sparse and non-symmetric. This increases the processing time and storage requirements. The computational advantage, which is gained by boundary discretization, is offset to the full and non-symmetric matrices [2]. Furthermore, the non-uniqueness problem occurs at characteristic wave numbers corresponding to interior problems [2, 3].

Different methods including the CHIEF method and the Burton-Miller method to overcome the non-uniqueness problem have been devised [1, 2, 3, 4]. In the CHIEF method, the integral formulation is modified by adding equations to enforce solutions to vanish at points in the interior. Thus, the fictitious solutions can be differentiated from the true one. But there is a lack of rigorous criteria for selecting interior points and determining the limit of stability [3]. The Burton-Miller method, in which the integral equation is combined with its normal derivative, theoretically precludes non-unique solutions. From a practical viewpoint, a disadvantage is the introduction of various orders of singular integrals of Green's function [4], which must be numerically described and can lead to inefficiencies in computation. During the past few decades, tremendous progresses in the development of BEM are moving the application of BEM in predicting sound radiation in infinite domain. For example, with the recent developments in fast multipole BEM [5], the computational efficiency is significantly improved. The relevant work of BEM is still on its way.

The standard FEM for predicting sound radiation in infinite domain remain two key challenges [1, 2, 3, 6]. How to treat the infinite domain and satisfy the Sommerfeld radiation condition at infinity is the first challenge. The other is the numerical dispersion issue with increasing wave number. In contrast to BEM, the infinite domain is usually truncated by an artificial boundary, yielding a finite computational domain. A non-reflecting boundary condi-

Received 23 April 2017,
accepted 16 November 2017.

© S. Hirzel Verlag · EAA

tion is imposed on the artificial boundary to replace the Sommerfeld radiation condition at infinity. Recent numerical treatments including absorbing boundary conditions, Dirichlet to Neumann (DtN) boundary conditions and perfectly matched layer (PML) have been proven to be effective approaches for handling sound radiating problems in unbounded domains [6]. Among these approaches, it has been shown that the DtN boundary condition, which relates the "Dirichlet datum" to the "Neumann datum" with the help of an integral operator, is an exact non-reflecting boundary condition [6]. Due to the decreased domain, the computation cost is greatly reduced. But the size of finite domain must be balanced by the ability to eliminate the spurious wave reflection with a computationally efficient and geometrically truncation boundary treatment [3].

It is well known that the accuracy of the numerical solutions will deteriorate rapidly as the frequency is increased [6]. A direct way of improving the accuracy is to refine mesh. However, the computational cost may be very expensive due to using the refined meshes. In order to reduce the numerical dispersion error, several techniques softening the "overly-stiff" property of the finite element model based on the smoothing technique or meshfree method have been developed in recent years to overcome the issue. In the advanced finite element method field, the novel weakened weakform based on G space theory is proposed by Liu and his colleagues to solve the partial differential equations in solid mechanics problems [7]. Based on the W2 form and the gradient smoothing technique from the meshfree methods, several outstanding methods have been devised for solid mechanics and acoustic problems, such as the meshfree cell-based smoothed alpha radial point interpolation method (CS-α RPIM)[8], the hybrid smoothed finite element method (HS-FEM)[6, 9], the stable node-based smoothed finite element method (SNS-FEM)[10], the edge-based smoothed finite element method (ES-FEM) [11] and the superconvergent alpha finite element method (SαFEM)[12]. Using these methods or techniques, the system stiffness is very properly softened and is closer to the exact one. Therefore, more accurate solution is achieved compared to the "overly-stiff" FEM.

The variable-order infinite acoustic wave envelope element (WEE) method [13, 14, 15, 16] is a numerical technique to properly model the amplitude decay of the outgoing travelling wave, which has been developed in the 1990s. The major advantage of WEE is the ease of dealing with exterior acoustic problems with infinite domains. There are no the singular integrals of Green's function and the non-uniqueness problem involved in BEM. As any other numerical method, WEE also has disadvantages. For radiators with complex geometric shapes, WEE must be coupled with conventional finite elements [17, 18, 19]. The WEEs are connected with the finite elements by element matching. Therefore, the WEEs must be reconstructed when the finite elements are changed, and the system equation corresponding to WEEs needs to be assembled again.

Meshfree methods are a relatively new approach in the field of numerical simulations compared with mesh-based methods. In general, meshfree methods can be categorized into three types according to the formulation procedures [20]: meshfree methods based on weak-forms such as the element-free Galerkin (EFG) method [21, 22, 23, 24], meshfree methods based on collocation techniques such as the meshfree collocation method with radial basis function (RBF) [25, 26] and meshfree methods based on the combination of weak-forms and collocation techniques [27, 28, 29]. In these methods, the problem domain and its boundary are modelled and represented by using sets of nodes scattered in the problem domain and on its boundary. A major characteristic of these methods is that mesh or connectivity of nodes, at least for field variable interpolations, is not required. A set of arbitrarily distributed nodes in the domain is only used to construct the shape functions [20]. In the meshfree methods, the moving least squares (MLS) approximation, the partition of unity method and the radial basis function (RBF) method are usually employed to construct the shape functions [20].

The meshfree point interpolation methods (PIM) [30] are proposed by Liu and Gu based on the Galerkin weakform. In PIM, the problem domain is represented by arbitrarily distributed nodes. The polynomial point interpolation method is employed to construct the shape functions based on a set of arbitrarily distributed nodes in a local domain. A set of background cells are needed to evaluate the integrals in the Galerkin weak-forms. The major features of PIM are that the shape functions possess Kronecker delta function property and that the essential boundary conditions can be easily enforced as in the finite element method (FEM). In the polynomial PIM, the moment matrix can be singular. This problem is overcome using a two-stage matrix triangularization algorithm (MTA) [31], which automatically excludes the nodes and the terms of the polynomial basis that are used in the formation of the moment matrix. However, the PIM based on the Galerkin weak-form is not robust for irregular nodal distributions due to the incompatible nature of the polynomial PIM shape functions. Too high order of polynomials that resulted from too many nodes used in the local support domain leads to a too drastic variation in the PIM shape functions [20].

The radial point interpolation method (PRIM) [32, 33] that uses RBF and is stable and robust for arbitrary nodal distributions is proposed and employed to overcome this singularity problem. The rate of convergence of this method is higher than that of the finite element method [20]. This method has been successfully applied to many problems, such as two-dimensional (2D) and three-dimensional (3D) solid mechanics [32, 34], material non-linear problems in civil engineering [35], problems of smart materials [36], plate and shell structures [37] and so on. In addition, in the case of the Helmholtz equation, it has already been shown that PRIM provides accurate results for interior acoustic problems [38]. If the PRIM is employed to predict the acoustic pressure for exterior

acoustic problems with infinite domain, a set of arbitrarily distributed nodes are needed to represent the acoustic field, which is computationally very expensive and impractical. Considering the major advantage of WEE dealing with exterior acoustic problems in infinite domains, the idea of combining PRIM with WEE is naturally of great interest in acoustic radiation prediction in the infinite domain. In addition, it is very desirable and beneficial to combine the two methods to make use of their advantages while evading their disadvantages.

In this paper, the meshfree radial point interpolation method is introduced to compute acoustic fields in infinite domain. The infinite domain is divided into an inner domain and an outer domain, which are discretized by a set of arbitrarily distributed nodes and WEEs respectively. The RPIM is employed in the inner domain to improve the accuracy and soften the system stiffness, and WEE method is used to properly model the amplitude decay. The interface elements [39] are employed to achieve the coupling of meshfree and WEE and make the shape functions satisfy both the consistency and compatibility requirements on the interface. The singular integrals of Green's function and the non-uniqueness problem are eliminated in the proposed hybrid method compared to the BEM. In contrast to the FEM combined with WEE method, the system equation of the outer domain needs to be just assembled once, when the field nodes are increased in the inner domain to improve the calculation accuracy. For the same node degrees of freedom (NDoF), the devised method not only can provide data with high accuracy but also has a faster convergence speed than the method of FEM combined with WEE. Although the solution time of the proposed method is more than that of the FEM combined with WEE method for the same NDoF, better computational efficiency can be achieved compared with the FEM combined with WEE method under the same level of the accuracy. The present method is validated by simulations and experiments.

2. Theoretical background

The harmonic steady-state acoustic pressure field radiated by a closed radiator in an infinite acoustic fluid domain V can be described by the Helmholtz equation

$$\nabla^2 p(\mathbf{x}) + k^2 p(\mathbf{x}) = 0, \quad \mathbf{x} \in V, \tag{1}$$

where $k = \omega/c$ is the acoustic wavenumber, ω is the angular frequency of the harmonic vibration of the boundary surface S_b, and c is the speed of sound in the acoustic medium. The boundary condition at the surface of the vibrating structure is prescribed as

$$\nabla p(\mathbf{x}) \cdot \mathbf{n}_b = -\mathrm{i}k\rho c v(\mathbf{x}), \quad \text{on } S_b, \tag{2}$$

where $\mathrm{i}^2 = -1$, $v(\mathbf{x})$ is a prescribed normal velocity and $\mathbf{n}_b$ represents the normal vector on the boundary. The Sommerfeld radiation condition is

$$\lim_{r\to\infty} r^{\alpha}\left(\frac{\partial p(r)}{\partial r} + \mathrm{i}kp(r)\right) = 0, \tag{3}$$

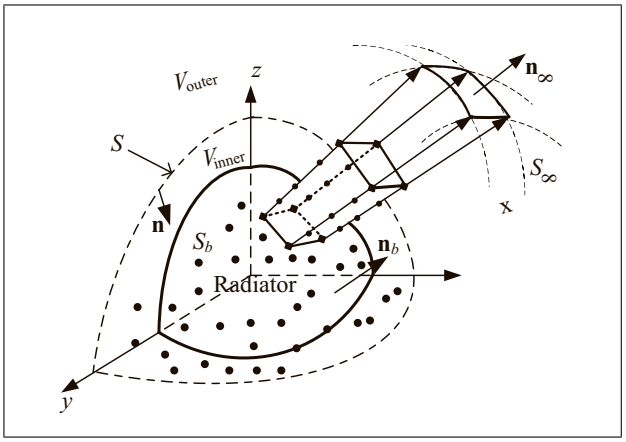


Figure 1. A radiating body in an infinite domain.

where r denotes a cylindrical or spherical polar radius, and α depending on the dimension of the domain, equals 1 or 2 for the 2D or 3D domain, respectively. At infinity, this is equivalent to stipulating the $\rho c-$impedance condition at a boundary, i.e.,$\nabla p \cdot \mathbf{n}_\infty + \mathrm{i}kp = 0$ when $\mathbf{x} \in S_\infty$.

The infinite domain V surrounding the radiator is divided into an inner domain V_{inner} and an outer unbounded domain V_{outer}, and they are separated by an interface S_γ, as shown in Figure 1. A set of arbitrarily distributed discrete field nodes is used to represent the inner domain V_{inner}. The outer domain V_{outer} is discretized by one layer of variable-order infinite acoustic wave envelope elements.

It is assumed that the radiated acoustic pressure on S_γ satisfies the condition of this form

$$\frac{\partial p}{\partial \mathbf{n}_\gamma} = -\mathrm{i}k\rho c\frac{p}{Z}, \tag{4}$$

where $\mathbf{n}_\gamma$ is outward normal on S_γ for V_{outer}, and Z is the unknown radiation impedance. Let $p^h(\mathbf{x})$ represent the trial function of the acoustic pressure. Application of the weighted residual formulation to Equation (1) for the inner and outer domain respectively yields

$$\int_{V_{\text{inner}}} \nabla W \cdot \nabla p^h \,\mathrm{d}V - k^2 \int_{V_{\text{inner}}} W p^h \,\mathrm{d}V - \mathrm{i}k\rho c \int_{S_b} W v(\mathbf{x}) \,\mathrm{d}S - \mathrm{i}k\rho c \int_{S_\gamma} W \frac{p^h}{Z} \,\mathrm{d}S = 0 \tag{5}$$

and

$$\int_{V_{\text{outer}}} \nabla W \cdot \nabla p^h \,\mathrm{d}V - k^2 \int_{V_{\text{outer}}} W p^h \,\mathrm{d}V - \int_{S_\infty} W \frac{\partial p^h}{\partial \mathbf{n}_\infty} \,\mathrm{d}S + \mathrm{i}k\rho c \int_{S_\gamma} W \frac{p^h}{Z} \,\mathrm{d}S = 0, \tag{6}$$

where W is the weighting function in the weighted residual formulation

3. Inner domain

3.1. The shape function and weighting function

In the inner domain, the radial point interpolation method (RPIM) is employed to form the shape function of the

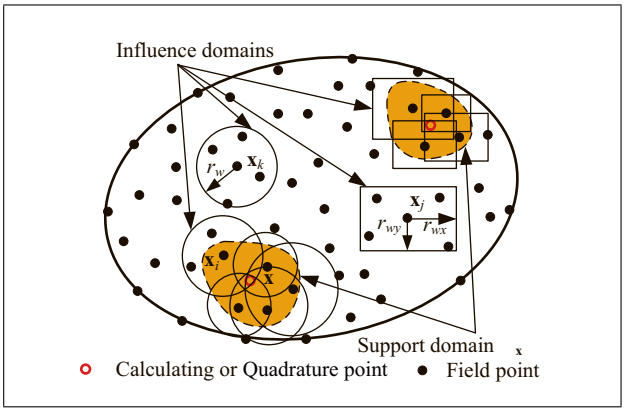


Figure 2. Influence domain of field node $\mathbf{x}_I$ and support domain of calculating point $\mathbf{x}$.

acoustic pressure. The RPIM interpolation augmented with polynomials of the acoustic pressure $p(\mathbf{x})$ can be written as [20]

$$\begin{aligned} p^h(\mathbf{x}) &= \sum_{i=1}^{n} R_i(\mathbf{x})a_i + \sum_{j=1}^{m} p_j(\mathbf{x})b_j \\ &= \mathbf{R}^{\mathrm{T}}(\mathbf{x})\mathbf{a} + \mathbf{p}^{\mathrm{T}}(\mathbf{x})\mathbf{b}, \end{aligned} \tag{7}$$

where $\mathbf{a}^{\mathrm{T}} = [a_1, a_2, \cdots, a_n]$ and $\mathbf{b}^{\mathrm{T}} = [b_1, b_2, \cdots, b_m]$ are the unknown constant coefficient vectors, $R_i(\mathbf{x})$ is a radial basis function (RBF), n is the number of RBFs, $p_j(\mathbf{x})$ is monomial in the space coordinates $\mathbf{x}^{\mathrm{T}} = [x, y, z]$, m is the number of polynomial basis functions, $\mathbf{R}^{\mathrm{T}} = [R_1(\mathbf{x}), R_2(\mathbf{x}), \ldots, R_n(\mathbf{x})]$ and $\mathbf{p}^{\mathrm{T}} = [p_1(\mathbf{x}), p_2(\mathbf{x}), \ldots, p_m(\mathbf{x})]$. The polynomial term is not always included in Equation (7). In case of $m = 0$, pure RBFs are used. Studies have indicate that adding polynomial terms can improve the accuracy and stability of numerical calculation, reduce the sensitivity of shape parameters and provide us much more freedom and wider range in choosing shape parameters [20]. Multi-quadrics, Gaussian and Thin Plate Spline are the most com monly used RBFs.

$$\begin{cases} \text{Multi-quadrics(MQ)}: & R_i(\mathbf{x}) = \left(r_i^2 + (\alpha_c d)^2\right)^q, \\ \text{Gaussian(EXP)}: & R_i(\mathbf{x}) = \mathrm{e}^{-\alpha_c (r_i/d)^2}, \\ \text{Thin Plate Spline(TPS)}: & R_i(\mathbf{x}) = r_i^{\eta}, \end{cases} \tag{8}$$

where $\alpha_c \geq 0$, q and η are the shape parameters, the characteristic length d denotes the average nodal spacing in the local support domain of the point of interest $\mathbf{x}$, and $r_i = \sqrt{(x - x_i)^2 + (y - y_i)^2 + (z - z_i)^2}$ is the distance between the i*th* point $\mathbf{x}_i$ and the point of interest $\mathbf{x}$. Note that the radial basis function $R_i(\mathbf{x})$ is only the function of r_i. In using RBFs, the shape parameters need to be determined for good performance. They should be usually determined by numerical examinations for the given types of problems [20].

To determine $\mathbf{a}$ and $\mathbf{b}$ in Equation (7), n field nodes within the support domain $\Omega_{\mathbf{x}}$ of the interest point at $\mathbf{x}$ are used. To determine these field nodes, the influence domain is employed. The influence domain is defined as a domain for a field node that it has an influence upon, the centre of which is the field node [20]. When the calculating or quadrature point $\mathbf{x}$ is in the influence domain of the field node, this field node will be used to construct shape functions for the calculating or quadrature point. The difference between an influence domain and a support domain is shown in Figure 2. By enforcing these n nodes within the support domain satisfying Equation (7) and using the additional m equations $\sum_{i=1}^{n} p_j(\mathbf{x}_i)a_i = 0 (j = 1, 2, \ldots, m)$, the following set of equations in matrix form is formed:

$$\begin{bmatrix} \mathbf{p}_s \\ \mathbf{0} \end{bmatrix} = \underbrace{\begin{bmatrix} \mathbf{R} & \mathbf{P}_m \\ \mathbf{P}_m^{\mathrm{T}} & \mathbf{0} \end{bmatrix}}_{\mathbf{G}} \begin{bmatrix} \mathbf{a} \\ \mathbf{b} \end{bmatrix} = \mathbf{G} \begin{bmatrix} \mathbf{a} \\ \mathbf{b} \end{bmatrix}, \tag{9}$$

where the vector of acoustic pressure values $\mathbf{p}_s^{\mathrm{T}} = [p_1, p_2, \cdots, p_n]$, the matrix $\mathbf{R}$ is

$$\mathbf{R} = \begin{bmatrix} R_1(r_1) & R_2(r_1) & \ldots & R_n(r_1) \\ R_1(r_2) & R_2(r_2) & \ldots & R_n(r_2) \\ \vdots & \vdots & \ddots & \vdots \\ R_1(r_n) & R_2(r_n) & \ldots & R_n(r_n) \end{bmatrix}_{n \times n}, \tag{10}$$

and the matrix $\mathbf{P}_m$ is

$$\mathbf{P}_m = \begin{bmatrix} 1 & x_1 & y_1 & z_1 & \ldots & p_m(\mathbf{x}_1) \\ 1 & x_2 & y_2 & z_2 & \ldots & p_m(\mathbf{x}_2) \\ \vdots & \vdots & \vdots & \vdots & \ddots & \vdots \\ 1 & x_n & y_n & z_n & \ldots & p_m(\mathbf{x}_n) \end{bmatrix}_{n \times m} \tag{11}$$

Because $\mathbf{R}^{-1}$ usually exists for arbitrarily distributed nodes and the order of polynomial used in Equation (7) is relatively low, no singularity problem exists in the PRIM[20]. Solving Equation (10) for $[\mathbf{a}^{\mathrm{T}}, \mathbf{b}^{\mathrm{T}}]$ and substituting them into Equation (7) yields

$$p^h(\mathbf{x}) = \left[\mathbf{R}^{\mathrm{T}}(\mathbf{x}), \mathbf{p}^{\mathrm{T}}(\mathbf{x})\right] \mathbf{G}^{-1} \begin{bmatrix} \mathbf{p}_s \\ \mathbf{0} \end{bmatrix} = \mathbf{N}^{\mathrm{T}}(\mathbf{x})\mathbf{p}_s, \tag{12}$$

where $\mathbf{N}^{\mathrm{T}}(\mathbf{x}) = [N_1(\mathbf{x}), N_2(\mathbf{x}), \ldots, N_n(\mathbf{x})]$ are the RPIM shape functions corresponding to the nodal acoustic pressure vector. In the inner domain, the weighting function $W_i(\mathbf{x})$ is taken as $N_i(\mathbf{x})$.

3.2. Dimension of the influence domain

A circular or spherical influence domain of a field node $\mathbf{x}_i$ is characterized by the influence radius r_w. A box influence domain is represented by r_{wx} and r_{wy} in the x and y directions for 2D problems and r_{wx}, r_{wy} and r_{wz} in the x, y and z directions for 3D problems. For simplicity, $r_w = r_{wx} = r_{wy}$ or $r_w = r_{wx} = r_{wy} = r_{wz}$ is often used. r_w is defined as $r_w = \alpha_s d$[20], where α_s is the dimensionless size of the influence domain, and d is the nodal spacing near the field node at $\mathbf{x}_i$ [20].

The dimensionless size α_s of the influence domain heavily determines the actual dimension of the influence domain and should be pre-determined before analysis. For a class of problems, it is usually determined by carrying out numerical experiments [20].

4. Outer domain

In this section, a briefing for the variable-order infinite acoustic wave envelope element (WEE) method is given. A radiation function $p(r)$, for the domain exterior to a sphere $|r - r_0| = R$, can be expressed as an infinite series of the form [15]

$$p(r) = \frac{\mathrm{e}^{-\mathrm{i}kr}}{r} \sum_{n=0}^{\infty} \frac{f_n(\theta, \phi)}{r^n}, \tag{13}$$

where (r, θ, ϕ) are spherical coordinates relative to the origin r_0. The infinite series converges absolutely and uniformly in r, θ and ϕ in any domain $r \geq R+\epsilon > R$. Considering only the first m terms of this series, we obtain the approximate solution. To imitate the acoustic radiation characteristics in the infinite domain, one layer of WEEs are used to satisfy the Sommerfeld radiation condition. The infinite acoustic wave envelope elements take the form of elongated quadrilaterals (for 2D problems) or blocks (for 3D problems) that extend to infinity in the radial direction. They map from the orthogonal rectangles and blocks of side 2 in the parent *s*-*v* and *s*-*v*-*t* spaces [13, 14, 15, 16], respectively. Figure 3 shows both the parent and mapped elements.

The domain of the wave envelope element is defined by the position of eight geometry nodes *I*, *II*, *III*, *IV*, *V*, *VI*, *VII* and *VIII* which map from the points *I*(-1,-1,-1), *II*(-1,1,-1), *III*(1,1,-1), *IV*(1,-1,-1), *V*(-1,-1,0), *VI*(-1,1,0), *VII*(1,1,0) and *VIII*(1,-1,0) in the parent space. The four geometric nodes, *I*, *II*, *III* and *IV*, are placed on the interface S_γ. Nodes *V*, *VI*, *VII* and *VIII* are placed at distances a_I, a_{II}, a_{III} and a_{IV} from nodes, *I*, *II*, *III* and *IV* along the infinite sides. Note that the radial infinite edges must be divergent when defining these eight geometry nodes. The nodes (-1,-1, 1), (-1,1,1), (1,1,1) and (1,-1,1) in the parent element map to infinity in the mapped element.

The inverse infinite mapping along each infinite edge is of the form [16]

$$t = 1 - 2\frac{a_i}{r} \quad (i = I, II, III, IV), \tag{14}$$

where r is the distance along *I*-*V*, *II*-*VI*,*III*-*VII* or *IV*-*VIII* sides measured from the fictitious point 1′,2′,3′ or 4′ in the mapped element. Thus, an interpolation of the polynomial shape functions of the pressure p in the radial t direction of the parent element will yield a $1/r^n$ expansion in the real element. Therefore, an appropriate amplitude decay of the acoustic pressure can be achieved by using the nth-order Lagrangian polynomial, which is determined by n acoustic nodes equally spaced between the geometry nodes, in the radial t direction of the parent element.

The trial functions of the acoustic pressure are interpolated by the shape $\{\varphi(\mathbf{x})\}$ functions

$$p^h_{\mathrm{WEE}}(\mathbf{x}) = \{\varphi(\mathbf{x})\}\,\{p\}\,. \tag{15}$$

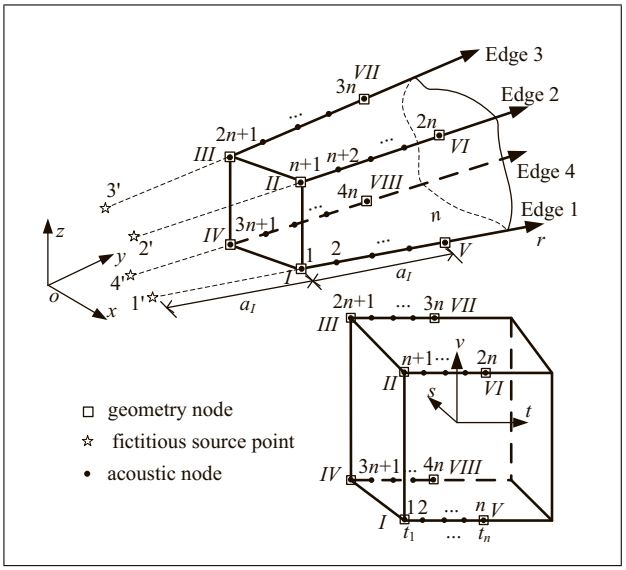


Figure 3. Infinite geometry mapping.

The radial component of $\varphi(\mathbf{x})$ is given as [16]

$$\begin{cases} T_i^n(t) = \dfrac{\pi(t)}{\pi'(t_i)(t - t_i)}, \quad i = 1, 2, \cdots, n, \\ \pi(t) = \displaystyle\prod_{i=1}^{n+1}(t - t_i). \end{cases} \tag{16}$$

The periodic component of $\varphi(\mathbf{x})$ is

$$\begin{cases} \mathrm{e}^{\mathrm{i}k(r-a)} = \mathrm{e}^{\mathrm{i}k\mu(s,t)} = \mathrm{e}^{\mathrm{i}ka(s)(1+t)/(1-t)}, \\ a(s) = \displaystyle\sum_{i=I}^{IV} M_i(s, v, t) a_i \Big|_{t=-1}. \end{cases} \tag{17}$$

where $M_i (i = I, II, \cdots, IV)$ is the mapping functions [16]. The tangential component of $\varphi(\mathbf{x})$ is

$$\begin{aligned} S_1(s, v) &= (1 - s)(1 - v)/4 \quad \text{(Edge 1)}, \\ S_2(s, v) &= (1 - s)(1 + v)/4 \quad \text{(Edge 2)}, \\ S_3(s, v) &= (1 + s)(1 + v)/4 \quad \text{(Edge 3)}, \\ S_4(s, v) &= (1 + s)(1 - v)/4 \quad \text{(Edge 4)}. \end{aligned} \tag{18}$$

Consequently, the shape function expressed entirely in terms of the parent *s*-*v*-*t* co-ordinate is obtained for the wave envelope element of $4n$ acoustic degrees of freedom by combining the wave-like variation, the tangential and radial components,

$$\begin{cases} \varphi^n_{(h-1)n+i}(s, v, t) = S_h(s, v) T_i^n(t) \mathrm{e}^{-\mathrm{i}k\mu(s,t)}, \text{(Edge } h) \\ 1 \leq i \leq n, \quad h = 1, 2, 3, 4 \end{cases} \tag{19}$$

The complex conjugates of the shape functions are chosen as the weighting functions to eliminate the complex exponential factors in the integrands of the system matrix formulation and use quadrature numerical integration for the evaluation of the system matrices [13, 14, 15, 16]. Thus, the weighting function is [16]

$$W = G(t)\left(\varphi^n(s, v, t)\right)^* = G(t) S(s, v) T^n(t) \mathrm{e}^{\mathrm{i}k\mu(s,t)} \tag{20}$$

where $G(t) = ((1-t)/2)^2$ is a geometric weighting factor to ensure the finiteness of the integrals involved in the evaluation of the system matrices and to make the radiation integral on S_∞ vanish as the outer boundary approaches infinity.

5. Coupling of RPIM and WEE

5.1. Constructing shape functions in interface elements

The acoustic pressure on the interface S_γ must satisfy the consistency and compatibility requirement. Therefore, the acoustic pressure on S_γ for V_{inner} and V_{outer} should be equal, i.e., $p_{\text{inner}} = p_{\text{outer}}$ on S_γ. Because $p^h(\mathbf{x})$ obtained from Equation (12) differs with the pressure value $p^h_{\text{WEE}}(\mathbf{x})$ obtained from Equation (15) at the field point $\mathbf{x}$ along S_γ, the inner domain cannot be coupled directly with the outer domain along S_γ.

To satisfy the consistency and compatibility requirement, the interface elements [39] are used in the inner domain near the interface S_γ. These elements exist in a layer of the sub-domain V_I along the interface S_γ within the inner domain V_{inner}, as shown in Figure 4. In the interface elements, a hybrid acoustic pressure approximation is defined to construct the shape functions of the inner domain on S_γ, which possess the delta function property. In this paper, 8 nodal isoparametric interface elements are used.

The hybrid acoustic pressure approximation in the inner domain is defined as

$$p^h(\mathbf{x}) = \begin{cases} p^h_{\text{RPIM}}(\mathbf{x}) + \lambda(\mathbf{x})(p^h_{\text{FE}}(\mathbf{x}) - p^h_{\text{RPIM}}(\mathbf{x})), & \mathbf{x} \in V_I \\ p^h_{\text{RPIM}}(\mathbf{x}), & \mathbf{x} \in (V_{\text{inner}} - V_I) \end{cases} \tag{21}$$

where $p^h(\mathbf{x})$ is the acoustic pressure of a field point in V_{inner}, $p^h_{\text{RPIM}}(\mathbf{x})$ is the acoustic pressure given by Equation (12), $p^h_{\text{FE}}(\mathbf{x})$ is the acoustic pressure determined by finite element (FE) interpolation, and $\lambda(\mathbf{x})$ is equal to the sum of the FE shape functions of an interface element associated with these interface element nodes that are located on the interface S_γ, i.e.,

$$\begin{cases} p^h_{\text{FE}}(\mathbf{x}) = \sum_{i=1}^{8} \phi_i(\mathbf{x}) p_i \\ \lambda(\mathbf{x}) = \sum_{i=1}^{q} \phi_i(\mathbf{x}) \quad \mathbf{x} \in S_\gamma \end{cases} \tag{22}$$

where $N_i(\mathbf{x})$ is the RPIM shape function, $\phi_i(\mathbf{x})$ is the FE shape function, and q is the number of nodes located on S_γ for an interface element. According to the property of the FE shape functions, $\lambda(\mathbf{x})$ satisfies $\lambda(\mathbf{x}) = 1(\mathbf{x} \in S_\gamma)$ and $\lambda(\mathbf{x}) = 0(\mathbf{x} \notin V_I)$.

Thus, the new acoustic pressure approximation in V_{inner} can be rewritten as

$$p^h(\mathbf{x}) = \sum_i \tilde{N}_i(\mathbf{x}) p_i \tag{23}$$

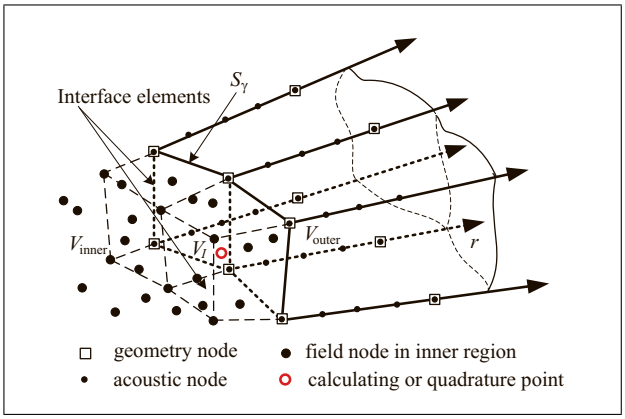


Figure 4. Interface elements used for coupling RPIM and WEE domains.

where

$$\tilde{N}_i(\mathbf{x}) = \begin{cases} \big(1 - \lambda(\mathbf{x})\big) N_i(\mathbf{x}) + \lambda(\mathbf{x}) \phi_i(\mathbf{x}), & \mathbf{x} \in V_I \\ N_i(\mathbf{x}), & \mathbf{x} \in (V_{\text{inner}} - V_I) \end{cases} \tag{24}$$

Clearly, the consistency and compatibility are satisfied by the approximants. The acoustic pressure approximation is continuous from the inner domain to the outer domain. Thus, the inner domain and outer domain can be coupled directly based on the above approximants.

In the conventional finite element method coupled with WEE method, the WEEs must be connected with the finite elements by element matching. Therefore, the WEEs have to be reconstructed when the finite elements are changed to improve the calculation accuracy of acoustic pressure, and the system equation of the outer domain needs to be reassembled. However, in the proposed hybrid method, there is no connection between the arbitrarily distributed nodes in inner domain and the WEEs in outer region. Thus, the system equation of the outer domain needs to be just assembled once, although the field nodes are increased in the inner domain to improve the calculation accuracy.

5.2. The form of the discrete system equation of the inner domain

Because the shape functions on S_γ are continuous and the same for the inner domain and outer domain, the terms associated to the unknown radiation impedance in Equation (6) and Equation (7) are equal and of opposite signs and thus vanish. As a result of substituting Equation (23) into Equation (5), a set of simultaneous equations can be formulated in the form

$$\left[\mathbf{K}^{\text{RPIM}} - k^2 \mathbf{M}^{\text{RPIM}}\right] \left\{p^{inner}\right\} = \mathbf{F}^{\text{RPIM}} \tag{25}$$

where $\mathbf{K}^{\text{RPIM}}$ and $\mathbf{M}^{\text{RPIM}}$ are the acoustic stiffness and mass matrices, respectively, in the inner domain, $\mathbf{F}^{\text{RPIM}}$ is the acoustic forcing vector corresponding to the prescribed velocity input on the boundary surface of the radiator and $\left\{p^{inner}\right\}$ is the unknown nodal parameters of acoustic pressures in the inner region to be solved for.

In general, to evaluate the integrals, a set of global background cells is required [20]. Hence, these global integrations are expressed as a summation of integrals over these cells. Thus, the Gauss quadrature can be employed in each cell. Note that the background cells do not practically exist. They merely assist in determining the integration points. Therefore, the mesh of background cells is independent of the field nodes, which are used for the field variable approximation. To evaluate F_i^{RPIM}, the boundary surface S_b is discretized into a set of surface background cells. Numerical form of F_i^{RPIM} is given as

$$\begin{aligned} F_i^{\mathrm{RPIM}} &= \mathrm{i}k\rho c \sum_{l=1}^{n_b} \int_{S_l} \tilde{N}_i v(\mathbf{x})\, \mathrm{d}S \\ &= \mathrm{i}k\rho c \sum_{l=1}^{n_b} \sum_{h=1}^{n_s} \sum_{g=1}^{n_v} w_h w_g \tilde{N}_i v(s_h, v_g) \sqrt{\det(\mathbf{J}_l \mathbf{J}_l^{\mathrm{T}})}, \end{aligned} \tag{26}$$

where n_b is the number of surface background cells; n_s and n_v denote the number of Gauss integral points in s and v direction, respectively; $\mathbf{J}_l$ is the Jacobian matrix corresponding to the lth background cell; and w_h and w_g are the Gauss weighting factor for the Gauss points.

When the influence domains of the field node $\mathbf{x}_i$ and $\mathbf{x}_j$ do not overlap, K_{ij}^{RPIM} and M_{ij}^{RPIM} both are exactly zero. Based on that, the box influence domain is employed. The adaptive background cells are constructed by the influence domains of these field nodes. For example, the overlapping area between the influence domains of the field node $\mathbf{x}_i$ and $\mathbf{x}_j$ is used as background cell to determine the integration points, as shown Figure 5.

Then, the K_{ij}^{RPIM} and M_{ij}^{RPIM} are obtained over this overlapping area. To calculate the integrations, the cell is first mapped onto a regular element. Then, the Gauss quadrature scheme is used to numerically perform the integrations over the cells. Numerical forms of K_{ij}^{RPIM} and M_{ij}^{RPIM} are given as

$$\begin{aligned} K_{ij}^{\mathrm{RPIM}} &= \int_{V_o} \nabla \tilde{N}_i \nabla \tilde{N}_j \, \mathrm{d}V \\ &= \sum_{h=1}^{n_s} \sum_{g=1}^{n_v} \sum_{q=1}^{n_t} w_h w_g w_q \left[\frac{\partial \tilde{N}_i}{\partial s}, \frac{\partial \tilde{N}_i}{\partial v}, \frac{\partial \tilde{N}_i}{\partial t} \right] \left(\mathbf{J}^{-1}\right)^{\mathrm{T}} \mathbf{J}^{-1} \\ &\quad \cdot \left[\frac{\partial \tilde{N}_j}{\partial s}, \frac{\partial \tilde{N}_j}{\partial v}, \frac{\partial \tilde{N}_j}{\partial t} \right]^{\mathrm{T}} \|\mathbf{J}\| \end{aligned} \tag{27}$$

$$\begin{aligned} M_{ij}^{\mathrm{RPIM}} &= \int_{V_o} \tilde{N}_i \tilde{N}_j \, \mathrm{d}V \\ &= \sum_{h=1}^{n_s} \sum_{g=1}^{n_v} \sum_{q=1}^{n_t} w_h w_g w_q \tilde{N}_i \tilde{N}_j \, \|\mathbf{J}\| \,, \end{aligned} \tag{28}$$

where V_o is the overlapping area between the influence domains of the field node $\mathbf{x}_i$ and $\mathbf{x}_j$; n_s, n_v and n_t denote the number of Gauss integral points in s, v and t direction, respectively; $\mathbf{J}$ is the Jacobian matrix; and w_h, w_g and w_q are the Gauss weighting factor for the corresponding Gauss points.

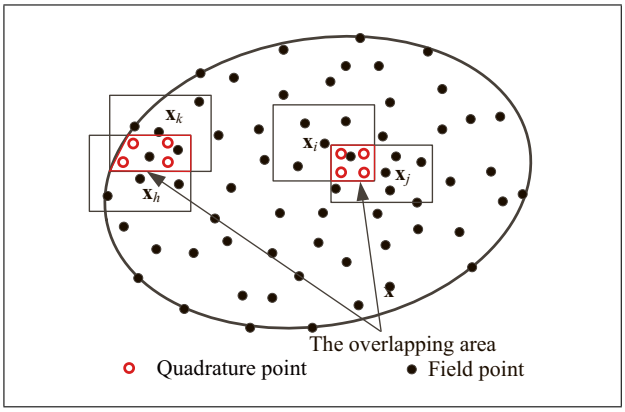


Figure 5. (Colour online) The adaptive Background cell for integral.

5.3. The form of the total discrete system equation

A set of simultaneous equations for wave envelope elements are given by

$$\left[\mathbf{K}^{\mathrm{WEE}} - k^2 \mathbf{M}^{\mathrm{WEE}}\right] \left\{p^{outer}\right\} = \{0\} \tag{29}$$

where $\mathbf{K}^{\mathrm{WEE}}$ and $\mathbf{M}^{\mathrm{WEE}}$ are the acoustic stiffness and mass matrices, respectively, in the outer domain. The discrete system equation of the outer domain is not associated with the arbitrarily distributed discrete field nodes within the inner domain. In the reference [13, 16], the form of them are given in detail.

Thus, the total system equation is obtained as

$$\left[\mathbf{K} - k^2 \mathbf{M}\right] \{p\} = \begin{bmatrix} \mathbf{F}^{\mathrm{RPIM}} \\ \mathbf{0} \end{bmatrix} \tag{30}$$

with

$$\mathbf{K}_{ij} = \begin{cases} K_{ij}^{\mathrm{RPIM}}, & \mathbf{x} \in V_{\mathrm{inner}} \\ K_{ij}^{\mathrm{WEE}}, & \mathbf{x} \in V_{\mathrm{outer}} \end{cases} \tag{31}$$

$$\mathbf{M}_{ij} = \begin{cases} M_{ij}^{\mathrm{RPIM}}, & \mathbf{x} \in V_{\mathrm{inner}} \\ M_{ij}^{\mathrm{WEE}}, & \mathbf{x} \in V_{\mathrm{outer}} \end{cases} \tag{32}$$

where $\mathbf{x}$ represents the quadrature point. It can be observed that the discrete system equation of the outer domain is not associated with the arbitrarily distributed discrete field nodes within the inner domain.

6. Numerical investigations

In what follows, acoustic radiations from an infinitely long cylinder of radius $R = 0.2$ m are investigated. The acoustic medium is air with its density $\rho = 1.21$ kg/m^3, and the speed of sound $c = 343$ m/s. The radiated acoustic pressure generated by the infinitely long cylinder are given in cylindrical co-ordinates as [16]

$$p(r, \theta) = -\mathrm{i}\rho c v(\theta) \mathrm{H}_n(kr) / H_n'(kR) \tag{33}$$

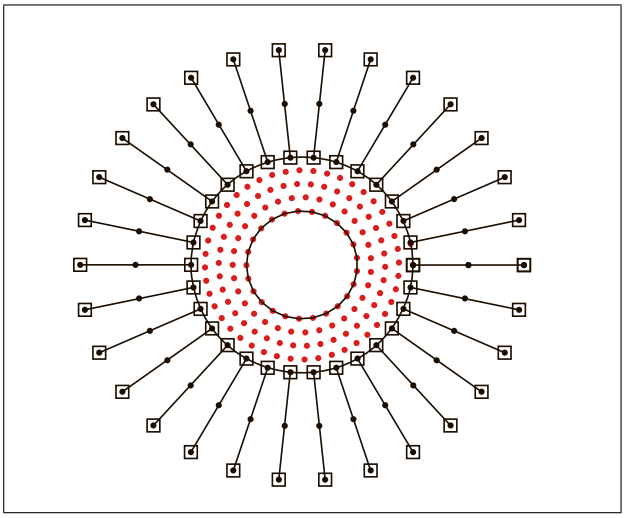


Figure 6. (Colour online) Diagram of meshfree combined with infinite acoustic wave envelope element for two-dimensional infinitely long cylinder radiation.

where H_n is the nth-order cylindrical Hankel function of the second kind and n corresponds to monopole, dipole and quadrupole radiation and equals to 0, 1 and 2, respectively, r is a cylindrical polar radius measured from the center of the cylinder, and θ is the cylindrical polar angle. $v(\theta) = v_0\cos(n\theta)$ is the corresponding normal velocity profiles on the boundary surface of the infinite cylinder, where v_0 is the velocity amplitude taken as 0.001 m/s.

The calculation frequency satisfies $kR = \pi/2$ in order to give an acoustical wavelength equal to the radius of the cylinder. With the aim of improving the accuracy of the predicted acoustic pressure, fictitious sources are located at the center of the cylinder in defining the topology of the infinite element according to the suggestion from Astley [13].

6.1. The shape parameters and the dimensionless size of the influence domain effect on accuracy

In this paper, $\epsilon_1(\%)$ and $\epsilon_2(\%)$ represent the relative errors of the real and imaginary components of the sound pressure, respectively. As indicated in the references [13, 16], third-order WEE can be used to correctly model the radial behavior of monopole, dipole and quadrupole radiation. The domain corresponding to $R \le r \le 2R$ is defined as inner domain, as shown in Figure 6. To study the effect of the shape parameters and the dimensionless size of the influence domain on the accuracy of the predicted acoustic pressure, 400 nodes combined with 120 third-order WEEs are used. For the monopole radiation, the maximum relative errors of the predicted acoustic pressure on the boundary surface nodes for different shape parameters with $\Delta\alpha_c = 0.1$ and $\Delta\eta = 0.1$ and α_s with $\Delta\alpha_s = 0.1$ are plotted in Figures 7, 8 and 9, where the linear polynomial is used in Equation (7).

These results show that the shape parameters have a remarkable influence on the accuracy of the predicted acoustic pressure and that the parameters must be carefully selected in RBFs to obtain good results. We observe that the prediction accuracy is relatively more sensitive to the shape parameters for EXP and TPS. For MQ and EXP,

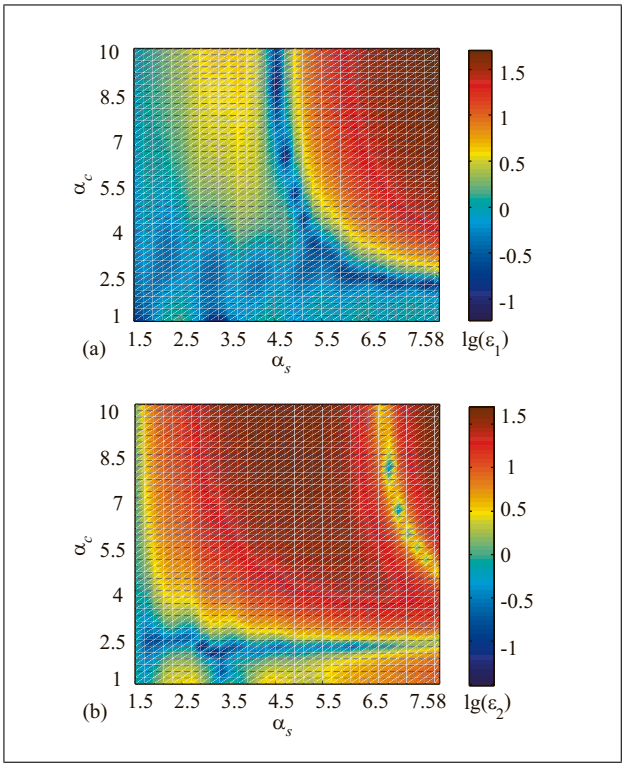


Figure 7. (Colour online) Variation of error of predicted acoustic pressure with α_c and α_s for EXP.

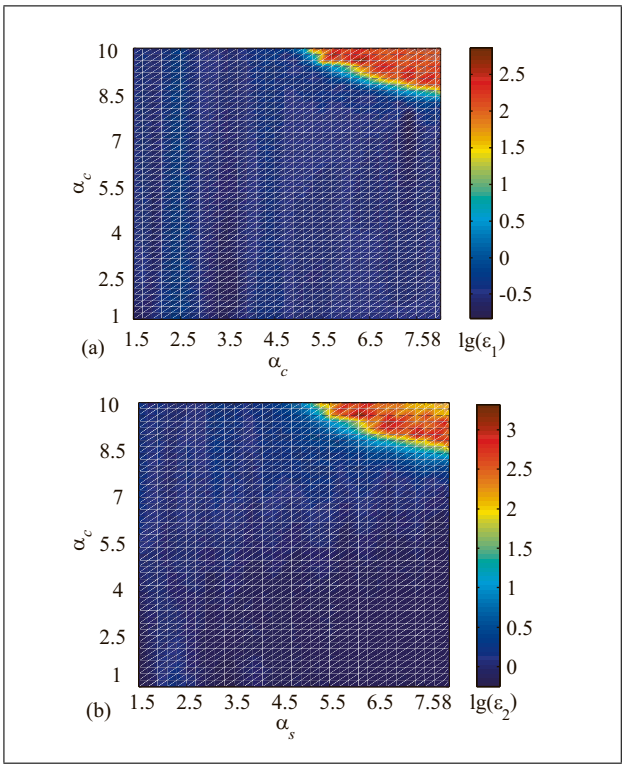


Figure 8. (Colour online) Variation of error of predicted acoustic pressure with α_c and α_s for MQ when $q = 1.03$.

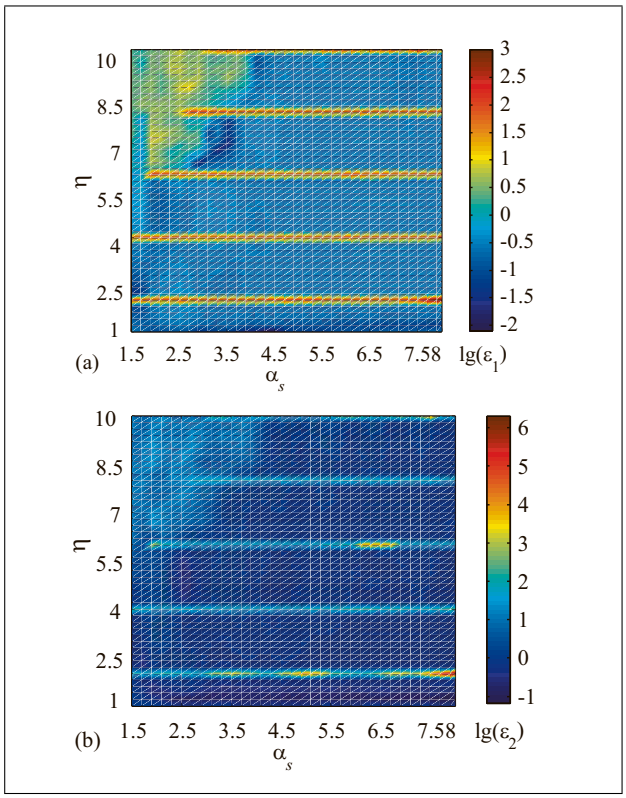


Figure 9. (Colour online) Variation of error of predicted acoustic pressure with η and α_s for TPS.

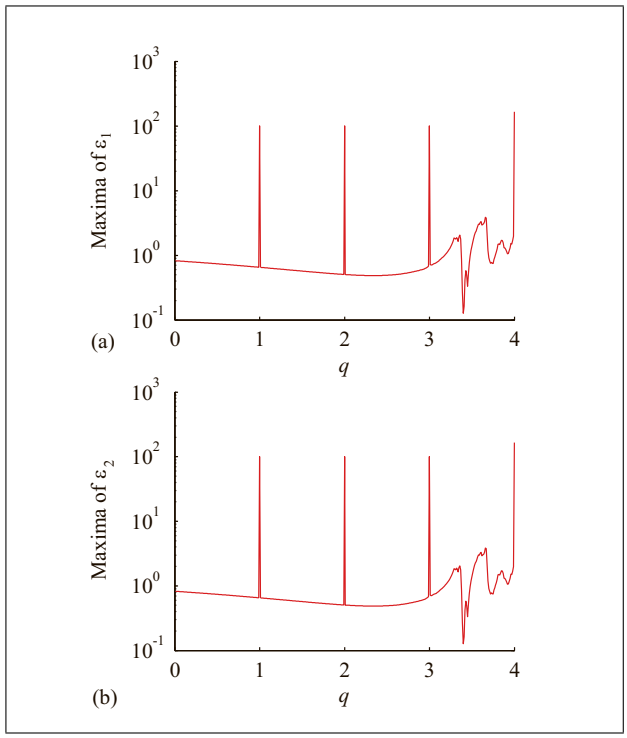


Figure 10. Variation of error of predicted acoustic pressure with q for MQ when $\alpha_c = 2.5$ and $\alpha_s = 2.5$.

it is better use $\alpha_c \leq 8$ and $1 \leq \alpha_c \leq 3$, respectively. α_c in the ranges can lead to satisfactory results. For TPS, η should be in the range of $1 \sim 6$. In addition, when η is near $2j(j = 1, 2, 3, \ldots)$, the condition number of the RPIM matrix $\mathbf{G}$ is large. Thus, the error will significantly increase due to the too large condition number of the matrix. The results corresponding to $\alpha_s \leq 1.5$ are not shown. The reason is that the RPIM matrix $\mathbf{G}$ is singular and the computation fails when the influence domain is too small($\alpha_s \leq 1.5$). It is also observed that the increase in the size of the influence domain cannot effectively improve the accuracy. However, the computational cost will increase remarkably if the influence domain becomes too large. Therefore, to ensure the predicted acoustic pressure results have high accuracy with no significant increase of the cost, it is better use $2 \leq \alpha_s \leq 3.5$. $\alpha_c = 2.5$, $\eta = 2.5$ and $\alpha_s = 2.5$ are used in the following investigation.

The parameter q has great influence on the performance of RPIM based on MQ [20]. To study the effect of the shape parameter q on the accuracy of the predicted acoustic pressure. the average ϵ_1 and average ϵ_2 on boundary surface are used, which are defined defined as

$$\begin{cases} \text{Average } \epsilon_1 = \dfrac{1}{N}\displaystyle\sum_{i=1}^{N}\left|\dfrac{\text{real}(p_i^h - p_i)}{\text{real}(p_i)}\right| \times 100\% \\ \text{Average } \epsilon_2 = \dfrac{1}{N}\displaystyle\sum_{i=1}^{N}\left|\dfrac{\text{imag}(p_i^h - p_i)}{\text{imag}(p_i)}\right| \times 100\% \end{cases} \tag{34}$$

where N is the number of nodes on the boundary surface, p_i and and p_i^h are the exact value and the approximated value of the sound pressure in the ith node, respectively. They are obtained for different q and shown in Figure 10.

It can be seen the prediction accuracy changes with q. When $q = 1$, 2, 3 and 4, the erroneous predicted sound pressure is obtained due to the singularity of the RPIM matrix $\mathbf{G}$. When $q \geq 3.5$, the error also increases due to the badly conditioned matrix $\mathbf{G}$. In this paper, $q = 2.3$ are used in the following investigation. Figures 11 and 12 show the average ϵ_1 and ϵ_2 on boundary surface for the dipole and quadrupole radiation, respectively, using the determined shape parameters and the dimensionless size. It is found that the determined shape parameters and the dimensionless size α_s lead to satisfactory results.

6.2. Convergence

The convergence of the method has been numerically studied using uniformly distributed nodes. The convergence curves are plotted in Figure 13 for monopole radiation, where d is the nodal spacing.

Based on the results, it can be observed that the accuracy of the results can be improved by decreasing d when TPS is used. However, the convergent processes corresponding to EXP and MQ are not very stable when more nodes are used. The shape parameters chosen in the RBFs affect the convergence rate and the accuracy of the RPIM method. Therefore, it is necessary to further tune the shape parameters.

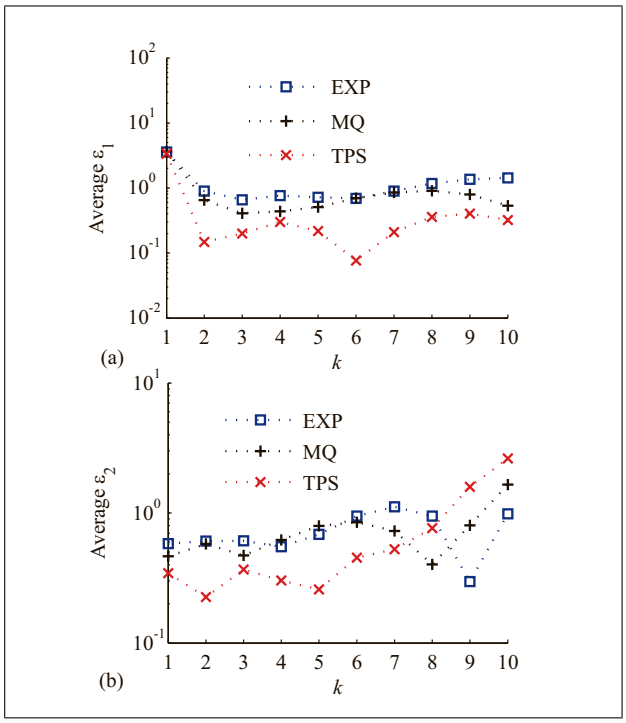


Figure 11. Variation of error of predicted acoustic pressure for dipole radiation.

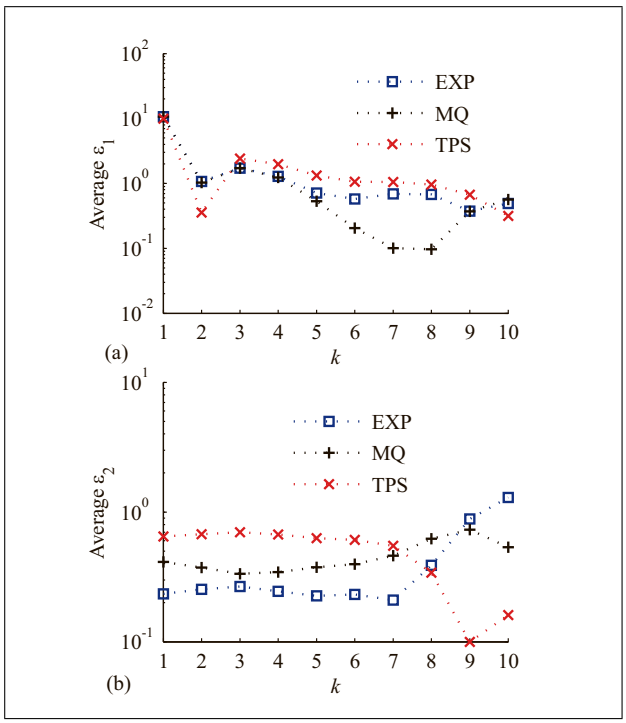


Figure 12. Variation of error of predicted acoustic pressure for quadrupole radiation.

6.3. Comparison between RPIM combined with WEE and FEM combined with WEE

For a comparison between the devised method and the FEM combined with WEE, both approaches are compared on a quadrupole radiation case. For each approach, the same configuration is used, as shown in Figure 14. The EXP is used as RBF in RPIM. The average prediction errors on the nodes of the boundary surface for different node degrees of freedom (NDoF) are shown in Figure 15 when $k = 2.5\pi$. The detailed values and the computational cost are shown in Table I.

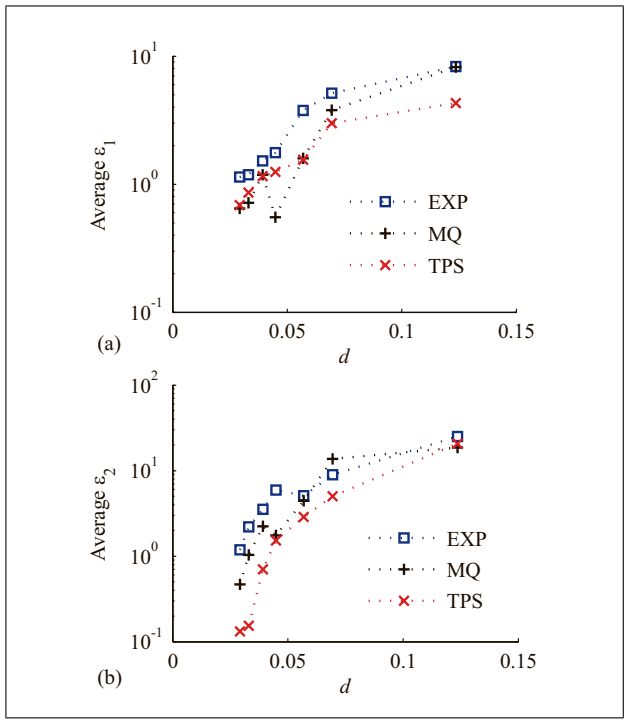


Figure 13. Variation of error of predicted acoustic pressure for monopole radiation with respect to the nodal spacing d.

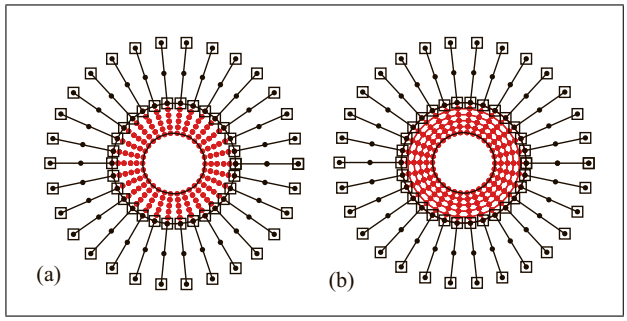


Figure 14. (Colour online) Configuration of two-dimensional monopole radiation (a) RPIM combined with WEE (b) FEM combined with WEE.

It is clear that the devised method not only can provide data with high accuracy but also has a faster convergence speed than the method of FEM combined with WEE. Under the same NDoF, it is observed that the solution time of the FEM combined with WEE method is less than the devised method. The reason is that the RPIM shape functions of the devised method must be reconstructed for these field nodes within the support domain of the calculating or quadrature point compared to the predetermined those of the finite element. However, the comparison of the computational cost should be performed for the same accuracy. Figure 16 shows the computational time for the same level

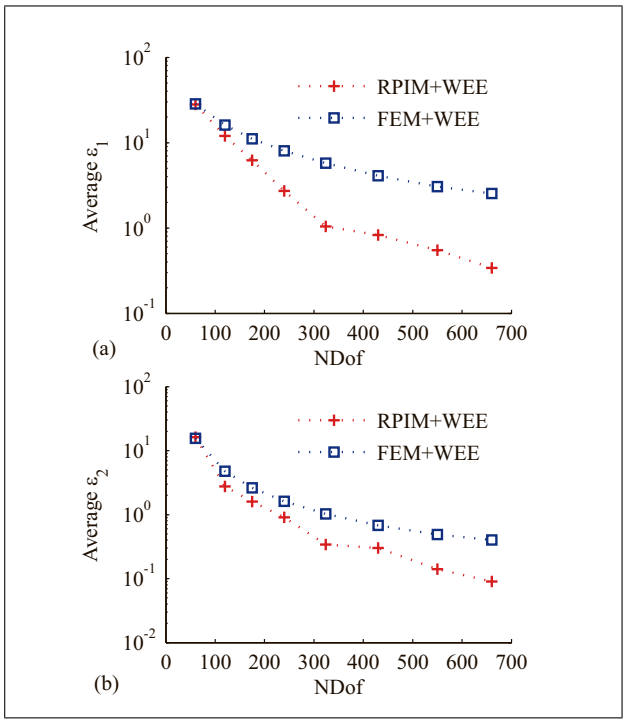


Figure 15. Prediction error for the devised method and the finite element combined with acoustic wave envelope element method.

Table I. Prediction error corresponding to RPIM+WEE and FEM+WEE.

NDoF	RPIM+WEE ε_1/%	RPIM+WEE ε_2/%	RPIM+WEE time/s	FEM+WEE ε_1/%	FEM+WEE ε_2/%	FEM+WEE time/s
60	27.99	16.19	1.29	28.58	15.58	0.91
120	12.01	2.77	3.11	16.08	4.78	2.17
175	6.22	1.60	10.29	11.14	2.63	6.99
240	2.73	0.91	20.16	8.05	1.62	13.56
324	1.04	0.34	38.84	5.74	1.03	27.13
430	0.83	0.30	64.68	4.09	0.68	45.64
550	0.55	0.14	119.53	3.06	0.49	91.81
660	0.34	0.09	139.92	2.54	0.40	117.41

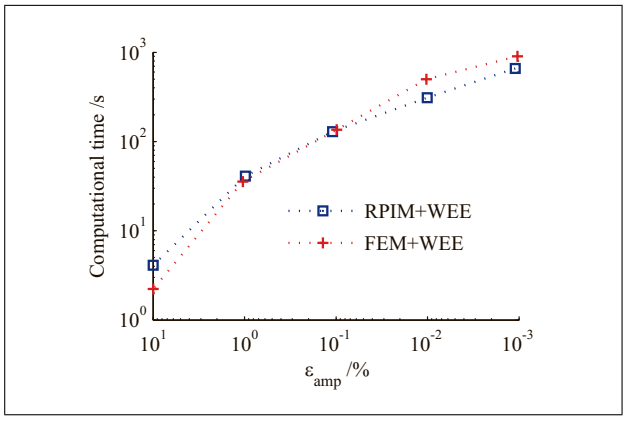


Figure 16. Computational cost for the same level of the accuracy.

of the accuracy, where ϵ_{amp} represents the relative error of the acoustic pressure amplitude.

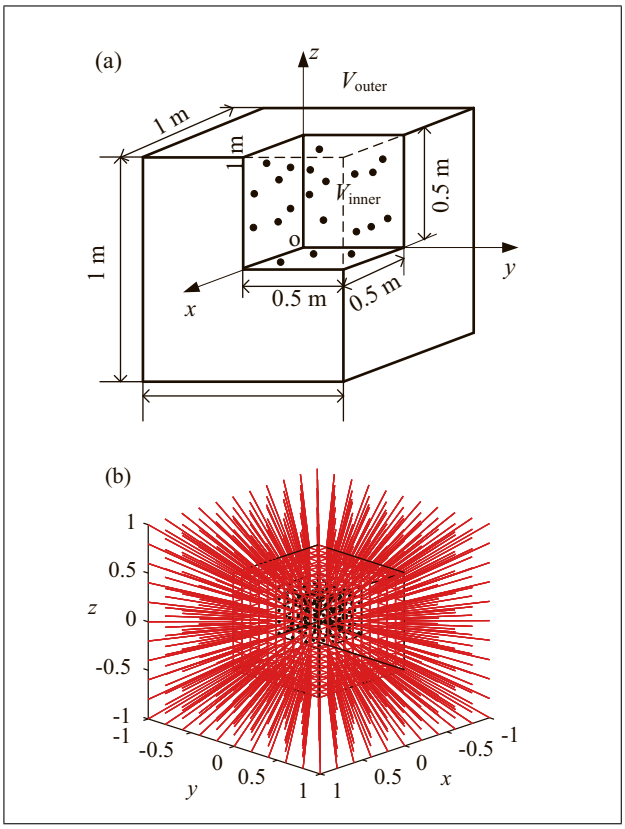


Figure 17. Shape and sizes of the designed structure.

The results indicate that the computational efficiency of the proposed method is better than that of the the FEM combined with WEE method when the error is less than 0.1%. The reason is that there is no connection in the proposed hybrid method between the arbitrarily distributed nodes in inner domain and the WEEs in outer region. The system equation of the outer domain needs to be just assembled once. It is convenient to improve the accuracy by just adding nodes in inner domain. In contrast to the proposed method, the WEEs are connected with the finite elements by element matching, which also increases the preprocessing time that is not included in the computation time. The WEEs have to be increased and reconstructed when the finite elements are refined to improve the calculation accuracy of acoustic pressure, and the system equation of the outer domain needs to be reassembled.

6.4. Application of this method

Acoustic radiations from a designed structure, the shape and sizes of which are shown in Figure 17a, are presented. Although there are no known analytical solutions for these structures, the exact solutions can be obtained using the substitute velocity boundaries, which are equivalent to those from a point source, that is, a simulation point source, in the structure. The prescribed normal velocity on the boundary surface is generated by placing an acoustic point source in the radiator. If the radiator vibrates under such a boundary condition, the radiated pressure must be equal to that generated by the point source. For this struc-

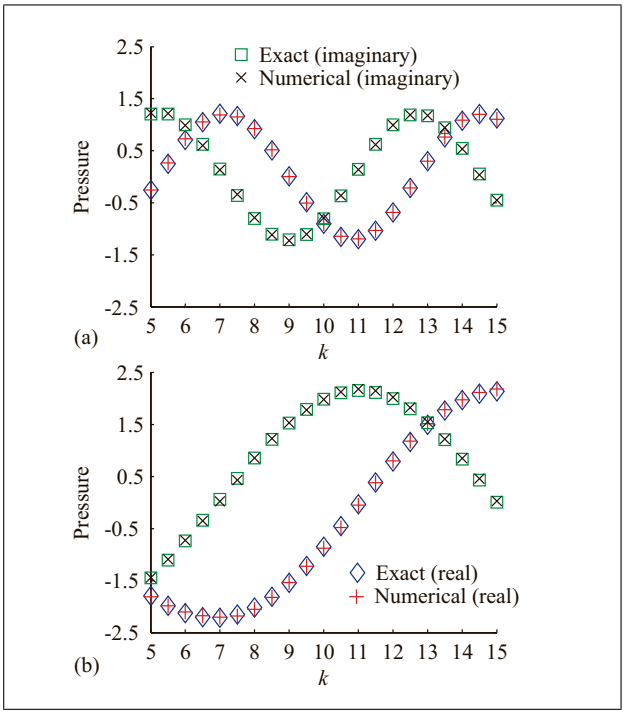


Figure 18. Variation of pressure in the selected field point with k (a) Field point P_1 (b) Field point P_2.

ture, a tripole is set at a fixed location with the coordinate $(-0.18, -0.18, -0.18)$.

The infinite domain V surrounding the structure is divided into an inner domain V_{inner} and an outer unbounded domain V_{outer}, as shown in Figure 17a. The numbers of arbitrarily distributed discrete field nodes used in V_{inner} and third-order WEE employed in V_{outer} are 300 and 600, respectively, as shown in Figure 17b. The EXP is selected as RBF in the RPIM. The radiated pressure is compared on an arbitrarily selected far field point $P_1 = (0, -1, 0)$ and a near field point $P_2 = (0, -0.5, 0)$. Figures 18 show the comparison results.

The comparison results show that the numerical solutions are consistent with the exact solutions. According to analysis, the maximum error of the predicted acoustic pressure is less than 2.34%. Thus, the accuracy of the predicted acoustic pressure by this method is acceptable.

7. Experimental investigation

To further validate the proposed method, the sound radiation of two radiators, namely, a cylindrical shell and a clamped plate are investigated experimentally, the physical data of which are shown in Table II. The cylindrical shell with flanges of 1.5 cm thickness welded at its both ends is fixed on a still frame by bolt to approximate the clamped boundary condition, as shown in Figure 19a. Both ends of the cylindrical shell are sealed by two aluminum alloy end plates with a thickness of 2 cm. This material is chosen because of its high stiffness and low weigh. An ordinary 10 inch loudspeaker is positioned on an end plate to generate an interior sound field, as shown in Figure 19c. The

Table II. Physical data of two radiators.

	Cyl. shell	Cla. plate
Length(m)	0.60	0.50
External diameter(m)	0.35	
Width(m)		0.50
Thickness(mm)	1.5	1.8
Density(kg/m^3)	7900	7800
Young′ modulus(N/m)	1.95×10^{11}	2.1×10^{11}
Poisson Ratio	0.247	0.30
Loss factor	$10^{-4} \sim 10^{-3}$	$10^{-5} \sim 10^{-3}$

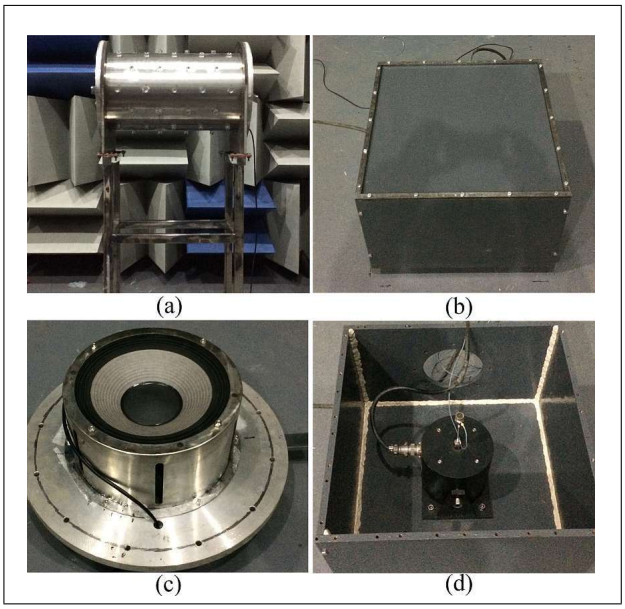


Figure 19. (a) Steel cylindrical shell (b) Clamped plate(c) Loudspeaker and its installation (d) Exciter and its installation.

interior sound field excited the cylindrical shell and the resulting structural vibrations caused an exterior sound field around the cylindrical shell. The stiff plate is fixed with his rim on a stiff frame, the bottom of which holds an exciter, using bolt to approximate the clamped boundary condition, as shown in Figure 19b. The exciter is connected to the center of the plate via a stiff push rod, as shown in Figure 19d, and makes the plate vibrate to generate an exterior sound field.

The surfaces of the cylindrical shell and the clamped plate are divided evenly divided into 30 and 25 elements, respectively. The normal velocities on the nodes and centers of the elements and the radiated acoustic pressure in the selected field points as depicted in Figure 20 are obtained by means of velocity and pressure measurements, as shown in Figure 21. The measurements are made from 100 Hz to 700 Hz for the cylindrical shell and 100 Hz to 500 Hz for the clamped plate with increment of 10 Hz, the lower limit being imposed by the semi-anechoic laboratory. The loudspeaker and the exciter are driven with sinusoidal signal. The initial values of input voltage and current for the loudspeaker are 15 V and 1.6 A, and the initial values for the exciter are 1.5 V and 2.7 A, where both

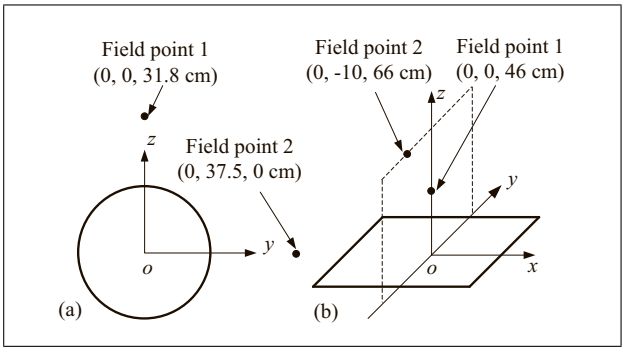


Figure 20. Coordinates of these field points (a) The cylindrical shell (b) The clamped plate.

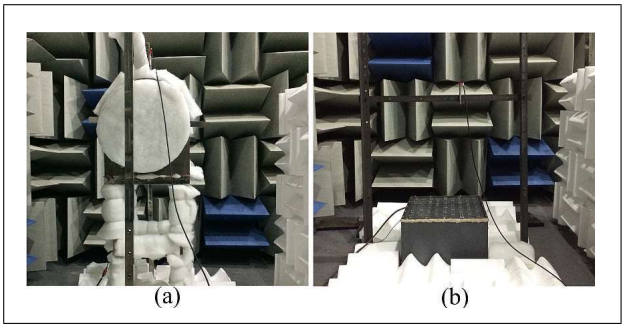


Figure 21. Acoustic pressure measurement (a) The cylindrical shell (b) The clamped plate.

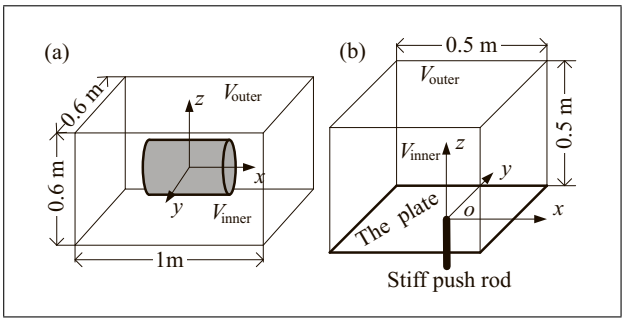


Figure 22. Divisions of infinite domain (a) The cylindrical shell (b) The clamped plate.

the input voltages remain constant when the frequency is increased. The instrumentation employed is listed in Table III. The mass ratio of the used accelerometer to the cylindrical shell or clamped plate is less than 1%. Thus, the accelerometer has little influence on the vibration of the radiator.

The divisions of exterior infinite domains of the two radiators are shown in Figure 22. In the proposed hybrid method, the numbers of evenly distributed discrete field nodes used in V_{inner} and third-order WEEs employed in V_{outer} are 200 and 160 for the cylindrical shell, 164 and 125 for the clamped plate. For the FEM combined with WEE method, 250 and 125 finite elements are employed in V_{inner} for the cylindrical shell and the clamped plate, respectively, and WEEs employed in V_{outer} are the same as those used in the proposed hybrid method. The measured

Table III. Instrumentation.

Device	Type
Sweep signal generator	DH 1301
Power amplifier	DH 5872
Accelerometer	LCO 158T
Data acquisition card	NI 9234
Microphone	B&K 4189

Table IV. Prediction error corresponding to RPIM+WEE and FEM+WEE.

Cylindrical shell	Field point 1		Field point 2	
Relative errors	$\epsilon_{\max}$	ϵ_{avg}	$\epsilon_{\max}$	ϵ_{avg}
RPIM+WEE	3.1	1.6	7.1	4.3
FEM+WEE	5.6	3.5	9.2	5.9
Clamped plate	**Field point 1**		**Field point 2**	
Relative errors	$\epsilon_{\max}$	ϵ_{avg}	$\epsilon_{\max}$	ϵ_{avg}
RPIM+WEE	15.0	6.1	14.7	5.1
FEM+WEE	16.7	8.4	17.7	11.6

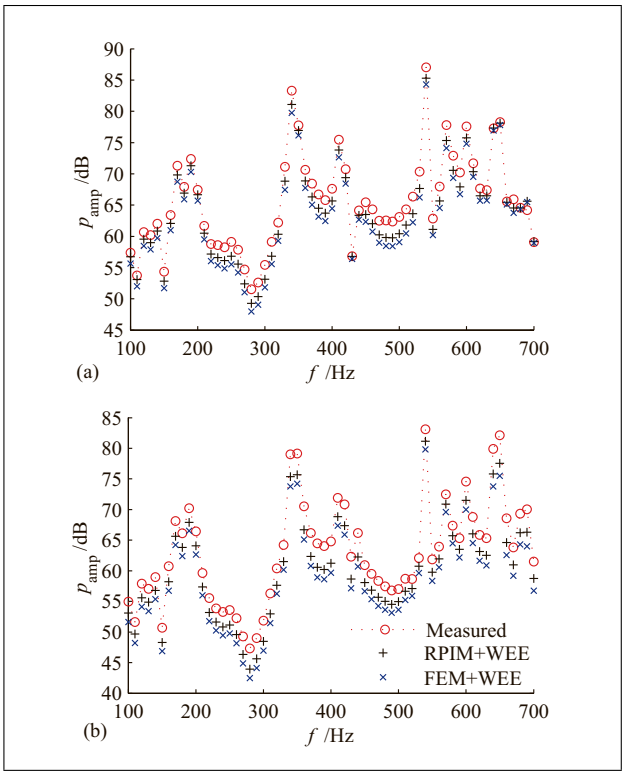


Figure 23. Amplitude of the acoustic pressure of the cylindrical shell at selected field points (a) Field point 1 (b) Field point 2.

and computed sound pressure levels are plotted in Figures 23 and 24 for the two radiators, respectively, where the EXP, $\alpha_c = 2.5$, $\alpha_s = 2.5$ and the the linear polynomial are employed and p_{amp} is used to represent the amplitude of the acoustic pressure. The detailed data of the calculation accuracy are shown in Table IV, where $\epsilon_{\max}$ and ϵ_{avg} represent the maximum and average values of the relative errors, respectively.

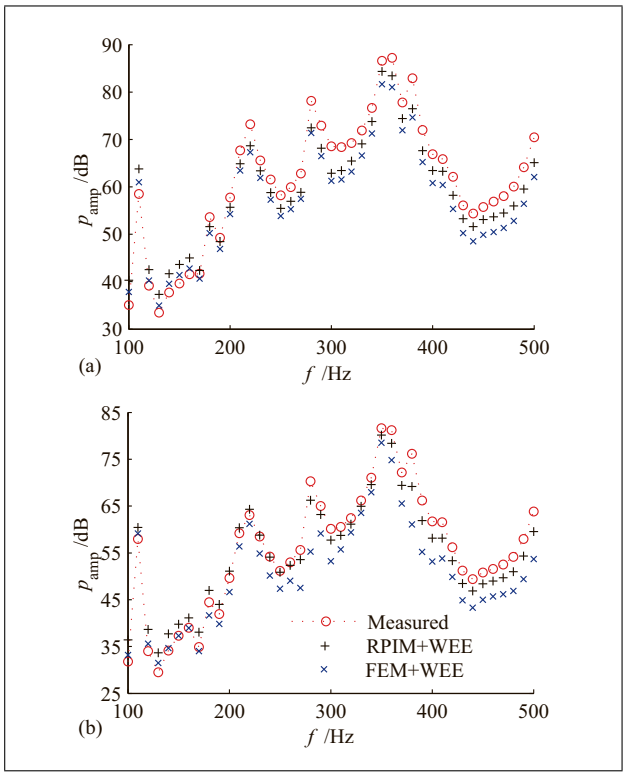


Figure 24. Amplitude of the acoustic pressure of the clamped plate at selected field points (a) Field point 1 (b) Field point 2.

The curves and the data show that the computed pressures by the proposed hybrid method are consistent with the measured values and have better accuracy than those by the FEM combined with WEE. From the data of the relative errors, the average error of the proposed hybrid method corresponding to the cylindrical shell is less than 4.3% and the maximum error is 7.1%. Thus, the accuracy of the computed acoustic pressure is good. For the clamped plate, the accuracy is lower than that corresponding to the shell. The average error is still acceptable, although the accuracies of the computed results in very few frequencies are not good. When the vibration velocity and acoustic pressure are measured, all of the accelerometer bases have been bonded to the surface of the clamped plate. Its surface shape is changed by these bases. When the radiated pressure is computed, the surface is still treated as plane. Its surface area is smaller than that of the cylindrical shell. In addition, there is still a reflection of sound wave. These cause discrepancy between the computed acoustic pressure and measured value in several frequencies and result in poor accuracy compared with the cylindrical shell.

8. Conclusions

The meshfree RPIM is successfully introduced to compute acoustic fields in infinite domain. A new method that combines the RPIM method with the variable-order infinite acoustic wave envelope element has been developed to predict acoustic pressure in the infinite domain. The factors having influence on the accuracy of the predicted acoustic pressure have been investigated. The shape parameters have significant effects on the accuracy of the predicted acoustic pressure. The available shape parameters have been determined in this paper by numerical experiments. The dimensionless size of the influence domain should be in the range of $2 \sim 3.5$. The developed method not only can supply results with high accuracy but also present excellent performance in convergence when compared to the conventional method of coupling FEM with WEE. Better computational efficiency can be achieved compared with the FEM combined with WEE method under the same level of the accuracy. The numerical results of the designed structure further indicate that the accuracy of the predicted acoustic pressure by this method is good. The experimental results show that the computed pressures are consistent with the measured values. In summary, this method can take full advantage of both the RPIM and WEE methods. It can thus be stated that this method is a valuable approach to predict acoustic pressure for exterior acoustic problems in the infinite domain.

Acknowledgement

This work was supported by the National Natural Science Foundation of China (“Research on structure sound radiation matrix deriving, computing and optimizing”, Grant No.51079118; “Research on computational auditory scene analysis based internal combustion engine noise sources identification”, Grant No.51279148).

References

[1] I. Harari, T. J. R. Hughes: Galerkin/least-squares finite element methods for the reduced wave equation with nonreflecting boundary conditions in unbounded domains. Comput. Methods Appl. Mech. Eng. **98**(3) (1992) 411–454.

[2] I. Harari, T. J. R. Hughes: A cost comparison of boundary element and finite element methods for problems of time-harmonic acoustics. Comput. Methods Appl. Mech. Eng. **97**(1) (1992) 77–102.

[3] L. L. Thompson: A review of finite-element methods for time-harmonic acoustics. J. Acoust. Soc. Am. **119**(3) (2006) 1315–1330.

[4] R. Visser: A boundary element approach to acoustic radiation and source identification. Enschede, The Netherlands: University of Twente, 2004.

[5] J. Y. Gong, J. Y. An, L. Ma, H. T. Xu: Numerical quadrature for singular and near-singular integrals of boundary element method and its applications in large-scale acoustic problems. Acta Ac. **41**(5) (2016) 768–775.

[6] Y. B. Chai, W. Li, Z. X. Gong, T. Y. Li: Hybrid smoothed finite element method for two-dimensional under water acoustic scattering problems. Ocean Eng. **116** (2016) 129–141.

[7] G. R. Liu, G. Y. Zhang: Smoothed point interpolation methods: G space theory and weakened weak forms. World Scientific, Singapore, 2013.

[8] G. R. Liu, G. Y. Zhang, Z. Zong, M. Li: Meshfree cell-based smoothed alpha radial point interpolation method (CS-ęÁ RPIM) for solid mechanics problems. Int. J. Comp. Meth. **10**(4) (2013) 1350020.

[9] Y. B. Chai, W. Li, Z. X. Gong, T. Y. Li: Hybrid smoothed finite element method for two dimensional acoustic radiation problems. Appl. Acoust. **103** (2016) 90–101.

[10] Y. B. Chai, W. Li, T. Y. Li, Z. X. Gong, X. Y. You: Analysis of underwater acoustic scattering problems using stable node-based smoothed finite element method. Eng. Anal. Bound. Elem. **72** (2016) 27–41.

[11] W. Li, Y. B. Chai, M. Lei, T. Y. Li: Numerical investigation of the edge-based gradient smoothing technique for exterior Helmholtz equation in two dimensions. Comput. Struct. **182** (2017) 149–164.

[12] Y. B. Chai, W. Li, G. R. Liu, Z. X. Gong, T. Y. Li: A superconvergent alpha finite element method (SęÁFEM) for static and free vibration analysis of shell structures. Comput. Struct. **179** (2017) 22–47.

[13] R. J. Astley, G. J. Macaulay: Mapped wave envelope element for acoustical radiation and scattering. J. Sound Vib. **170**(1) (1994) 97–118.

[14] R. J. Astley, G. J. Macaulay: Three-dimensional wave-envelope elements of variable order for acoustic radiation and scattering. Part I. Formulation in the frequency domain. J. Acoust. Soc. Am. **103**(1) (2007) 49–83.

[15] L. Cremers, K. R. Fyfe: On the use of variable order infinite wave envelope elements for acoustic radiation and scattering. J. Acoust. Soc. Am. **97**(4) (1994) 2028–2040.

[16] L. Cremers, K. R. Fyfe: A variable order infinite acoustic wave envelope element. J. Sound Vib. **171**(4) (1994) 483–508.

[17] A. Baghbani, D. Gregory-Smith: A new infinite element for unbounded water wave problems. Appl. Ocean Res. **25**(4) (2003) 213–223.

[18] J. C. Autrique, F. Magoules: Studies of an infinite element method for acoustical radiation. Appl. Math. Model. **30**(7) (2006) 641–655.

[19] C. X. Zheng: Error analysis of a coupled finite-infinite element method for an exterior Poisson problem. Appl. Numer. Math. **57**(57) (2007) 270–280.

[20] G. R. Liu, Y. T. Gu: An introduction to meshfree methods and their programming. Springer Verlag, The Netherlands, 2005.

[21] T. Belytschko, Y. Y. Lu, L. Gu: Element-free Galerkin methods. Int. J. Numer. Methods Eng. **37**(2) (1994) 229–256.

[22] T. Belytschko, Y. Y. Lu, L. Gu: Element free Galerkin methods for static and dynamic fracture. Int. J. Solids Struct. **32** (1995) 2547–2570.

[23] M. Peng, D. Li, Y. Chen: The complex variable element-free Galerkin (CVEFG) method for elasto-plasticity problems. Eng.Struct. **33**(1) (2011) 127–135.

[24] Z. Zhang, S. Hao, K. Liew, Y. Cheng: The improved element-free Galerkin method for two-dimensional elasto-dynamics problems. Eng. Anal. Bound Elem. **37**(12) (2013) 1576–84.

[25] S. Abbasbandy, H. R. Ghehsareh, I. Hashim: Numerical analysis of a mathematical model for capillary formation in tumor angiogenesis using a meshfree method based on the radial basis function. Eng. Anal. Bound Elem. **36**(12) (2012) 1811–1818.

[26] M. Dehghan, A. Shokri: A numerical method for solution of the two dimensional sine-Gordon equation using the radial basis functions. Math. Comput. Simul. **79**(3) (2008) 700–715.

[27] G. R. Liu, Y. T. Gu: Boundary meshfree methods based on the boundary point interpolation methods. Eng. Anal. Bound. Elem. **28**(5) (2004) 475–587.

[28] G. R. Liu, Y. L. Wu, H. Ding: Meshfree weak-strong (MWS) form method and its application to incompressible flow problems. Int. J. Numer. Meth. Fl. **40**(10) (2004) 1025–1047.

[29] Y. T. Gu, G. R. Liu: A meshfree weak-strong (MWS) form method for time dependent problems. **35**(2) (2005) 134–145.

[30] G. R. Liu, Y. T. Gu: A point interpolation method for two-dimensional solids. Int. J. Numer. Meth. Eng. **50**(4) (2001) 937–951.

[31] G. R. Liu, Y. T. Gu: A matrix triangularization algorithm for the polynomial point interpolation method. Comput. Method Appl. Mech. Engrg. **192**(19) (2003) 2269-2295.

[32] G. R. Liu, Y. T. Gu: A local radial point interpolation method (LR-PIM) for free vibration analyses of 2-D solids. J. Sound Vib. **246**(1) (2001), pp.29-46.

[33] J. G. Wang, G. R. Liu: A point interpolation meshless method based on radial basis functions. Int. J. Numer. Meth. Eng. **54**(11) (2002) 1623–1648.

[34] G. R. Liu, L. Yan, J .G, Wang, Y. T. Gu: Point interpolation method based on local residual formulation using radial basis functions. Struct. Eng. Mech. **14**(6) (2002) 713–732.

[35] J. G. Wang, G. R. Liu, P. Lin: Numerical analysis of Biot's consolidation process by raidal point interpolation method. Int. J. Solids Struct. **39**(6) (2002) 1557–1573.

[36] G. R. Liu, K. Y. Dai, K. M. Lim, Y. T. Gu: A radial point interpolation method for simulation of two-dimensinal piezoelectric structures. Smart Mater. Struct. **12**(2) (2003) 171–180.

[37] L. Liu, G. R. Liu, V. B. C. Tan: Element free method for static and free vibration ananlysis of spatial thin shell structures. Comput. Method Appl. Mech. Eng. **191**(51-52) (2002) 5923–5942.

[38] C. Wenterodt, O. V. Estorff: Optimized meshfree methods for acoustics. Comput. Methods Appl. Mech. Engrg. **200**(25) (2011) 2223–2236.

[39] Y. T. Gu, G. R. Liu: A coupled element free Galerkin/ boundary element method for stress analysis of two-dimensional solids. Comput. Methods Appl. Mech. Engrg. **190**(34) (2001) 4405–4419.